J Nanopart Res (2013) 15:1670
DOI 10.1007/s11051-013-1670-x

RESEARCH PAPER

Fabrication, characterization, and photocatalytic property of α-Fe_2O_3/graphene oxide composite

**Hong Li · Qidong Zhao · Xinyong Li ·
Zhengru Zhu · Moses Tade · Shaomin Liu**

Received: 5 December 2012 / Accepted: 19 April 2013 / Published online: 29 May 2013

Abstract Spindle-shaped microstructure of α-Fe_2O_3 was successfully synthesized by a simple hydrothermal method. The α-Fe_2O_3/graphene oxide (GO) composites was prepared using a modified Hummers' strategy. The properties of the samples were systematically investigated by X-ray powder diffraction (XRD), UV–Vis diffuse reflectance spectrophotometer, transmission electron microscope, atomic force microscope, X-ray photoelectron spectroscopy, and Raman spectroscopy (Raman) techniques. GO nanosheets act as supporting materials for anchoring the α-Fe_2O_3 particles. The average crystallite sizes of the α-Fe_2O_3 and α-Fe_2O_3/GO samples are ca. 27 and 24 nm, respectively. The possible growth of α-Fe_2O_3 onto GO layers led to a higher absorbance capacity for visible light by α-Fe_2O_3/GO than α-Fe_2O_3 composite. The photocatalytic degradation of toluene over the α-Fe_2O_3 and α-Fe_2O_3/GO samples under xenon-lamp irradiation was comparatively studied by in situ FTIR technique. The results indicate that the α-Fe_2O_3/GO sample synthesized exhibited a higher capacity for the degradation of toluene. The composite of α-Fe_2O_3/GO could be promisingly applied in photo-driven air purification.

Keywords α-Fe_2O_3 · Graphene oxide · In situ FTIR · Photocatalytic degradation · Toluene

Introduction

Graphene, a monolayer of carbon atoms with a tight packing of honeycomb lattice, has attracted immense research interest in nanotechnology in recent years (Geim and Novoselov 2007). Graphene exhibits outstanding properties such as very low resistivity, high mobility of charge carriers, optical, and electrical properties, and new quantum effect (Mukherjee and Kaloni 2012; Novoselov et al. 2005); which has been found to be useful in a variety of technological applications, including biotechnology (Dong et al.

H. Li · Q. Zhao · X. Li (✉)
State Key Laboratory of Fine Chemical, Key Laboratory of Industrial Ecology and Environmental Engineering (MOE), School of Environmental Science and Technology, Dalian University of Technology,
Dalian 116024, China
e-mail: xinyongli@hotmail.com; xyli@dlut.edu.cn

H. Li
Department of Basic, Dalian Naval Academy,
Dalian 116018, China

X. Li · M. Tade · S. Liu (✉)
Department of Chemical Engineering, Curtin University,
Perth, WA 6845, Australia
e-mail: shaomin.liu@curtin.edu.au

Z. Zhu
Research Center of Hydrology and Engineering, Academy of City and Environment, Liaoning Normal University,
Dalian 116029, China

2010; Guo et al. 2010; Liu et al. 2008; Yang et al. 2009), photocatalysis (Liang et al. 2010), and many energy storage devices (Pumera 2011) such as solar cells (Miao et al. 2012), supercapacitors (Chen et al. 2010b; Wang et al. 2010b), and lithium-ion batteries (LIBs) (Chou et al. 2010; Lee et al. 2010; Shen et al. 2011; Wang et al. 2009).

Graphene oxide (GO) was proven to be an effective and reliable precursor to produce graphene nanosheets owing to its low cost and massive scalability (Park and Ruoff 2009). Moreover, functionalized graphene-based materials can be prepared via chemical modification, which show unique electronic and optical properties as well as good biocompatibility (Akhavan et al. 2011; Sun et al. 2011). Since the creative work of Zhang et al. (2010a), who prepared a chemically bonded TiO_2 (P25)–graphene composite photocatalyst by a hydrothermal method, many efforts have been made to utilize the unique properties of graphene in order to increase the efficiency of photo conversion (Liu et al. 2010; Wang et al. 2010c; Yoo et al. 2011). Graphene and GO-based nanosheets could not only assist the dispersion of the metal oxide in aqueous media but also direct the self-assembly of metal oxides into nanostructures (Park and Ruoff 2009; Wang et al. 2010a; Wu et al. 2010). Notably, enhanced cycling performance for Li-ion battery has been observed with GO-supported Co_3O_4 nanoparticles or manganese oxide nanosheets (Wu et al. 2010; Zhang et al. 2011).

As an important n-type semiconductor, hematite (α-Fe_2O_3) has been widely used for gas sensors (Chauhan et al. 1999; Chen et al. 2005), water splitting (Cesar et al. 2006), photodetectors (Hsu et al. 2009), solar cells (Beermann et al. 2000), field-emission devices (Hsu et al. 2008; Yu et al. 2006), lithium-ion batteries (Liu et al. 2009; Nuli et al. 2008; Reddy et al. 2007; Wu et al. 2008), water purification (Song et al. 2012), and field-effect transistors (Fan et al. 2005). The α-Fe_2O_3 has also been selected as the support material for noble metal (Chen et al. 2005; Gou et al. 2008; Hu et al. 2007; Zhang et al. 2010b). Our group recently reported the photoelectric characteristics of α-Fe_2O_3 particles with hollow spindle shape (Li et al. 2012).

Considering that extensive research efforts have demonstrated that intriguing properties for various applications could be obtained by coupling functional nanoparticles with graphene derivatives (Chen et al. 2010a; Chou et al. 2010; Ji et al. 2011; Lee et al. 2010; Lian et al. 2010; Liang et al. 2010; Liu et al. 2010; Shen et al. 2011; Wang et al. 2009, 2010a, 2010b, 2011a, 2011b; Wu et al. 2010; Yang et al. 2009; Zhang et al. 2010a, 2011; Zhou et al. 2010; Zhu et al. 2011a, 2011b), we believe that it is interesting to explore more physical and chemical properties of different graphene-iron oxide composites. A number of recent reports have focused on the reduced GO-coupled Fe_2O_3 (Zhu et al. 2011a, 2011b) and graphene/Fe_3O_4 composites (Ji et al. 2011; Lian et al. 2010; Wang et al. 2011b; Zhang et al. 2010c; Zhou et al. 2010) for lithium-ion batteries. So far, only a few reports have been focused on the photo-induced performance of GO and α-Fe_2O_3 based composites. Meng et al. (2013) studied the hematite/reduced GO composites for photocatalytic water oxidation. They found that coupling the hematite nanoparticles with the reduced GO could greatly increase the photocurrent and reduce the charge recombination rate, which led to a higher O_2 evolution rate than α-Fe_2O_3 by a factor of two. Kim et al. (2012) reported an effective conducting scaffold of graphene–carbon nanotube composite for enhancing the photoelectrochemical water oxidation activity of hematite film. The delicate 3D-like architecture deriving from 1D carbon nanotube and 2D graphene formed a more open and highly exposed structure and effectively reduced the self-agglomeration of the carbon nanosheets, which could thus provide higher contact area between the conducting scaffold and Fe_2O_3 particles and also retain the intrinsic conducting ability of graphene and carbon nanotube for photoelectrochemical application. The above two instances reveal the attractive prospects of the photo-induced activity of graphene derivatives and α-Fe_2O_3-based composites.

In this work, we report the fabrication and the photocatalytic property of GO sheets-supported α-Fe_2O_3 microparticles in degrading a typical organic air pollutant. It is demonstrated that the α-Fe_2O_3/GO composite exhibited enhanced photo activity in terms of light absorption and photocatalytic degradation of toluene compared to the pure α-Fe_2O_3 counterpart.

Experimental

Synthesis of GO

GO was synthesized from graphite powder by a modified Hummers' method (Hummers and Offeman

1958), in which pre-oxidation of graphite was followed by oxidation according to Hummers' method. For the pre-oxidation, the graphite powder (4.0 g) was added with stirring into the concentrated H_2SO_4 (40 mL) solution in which $K_2S_2O_8$ (2.0 g) and P_2O_5 (2.0 g) were completely dissolved at 80 °C. The mixture, in a beaker, was kept at 80 °C for 4.5 h using an oil bath. Then, the mixture was cooled down and was diluted with 1 L of distilled deionized water. The pretreated product was filtered and washed until the pH of filtrate water became neutral. The shiny, dark-gray, pre-oxidized graphite was dried in air overnight. Then, it was dispersed by stirring into chilled H_2SO_4 (92 mL) in a flask in an ice bath. $KMnO_4$ (12 g) was added slowly with stirring to keep the temperature of reaction mixture below 20 °C. The resulting thick, dark green paste was allowed to react at 35 °C for 3 h followed by addition of H_2O (184 mL) to give a dark brown solution. After additional stirring for 2 h, the dark brownish solution was further diluted with distilled water (560 mL) and then H_2O_2 (30 %, 40 mL) was added slowly and the color of the mixture turned into brilliant yellow. The mixture was allowed to settle overnight and the supernatant was decanted. The remaining product was washed with 10 % HCl solution with stirring and the brownish solution was allowed to settle overnight. The supernatant was decanted and the remaining product was centrifuged and washed with deionized water. The washing process was repeated until the pH of the solution became neutral. After filtration and drying under vacuum, GO was obtained as a gray powder.

Synthesis of spindle-like α-Fe_2O_3

Spindle-shaped α-Fe_2O_3 particles were obtained via a hydrothermal route. $FeCl_3 \cdot 6H_2O$ (18 mmol) was added into distilled water (60 mL) to form a clear solution. Then 4.32 g urea (CH_4N_2O) and 9 mL ethylene glycol, a protective agent were added into the solution. Subsequently after magnetic stirring for 30 min at room temperature, the resultant solution was put into a Teflon-lined stainless steel autoclave of 100 mL capacity, which was sealed and maintained at 180 °C for 12 h. After cooling the autoclave to room temperature naturally, the obtained precipitate was collected by filtration, and then washed with absolute ethanol and distilled water in sequence for several times. The α-Fe_2O_3 product was dried in a vacuum box at 80 °C for 12 h.

Synthesis of the α-Fe_2O_3/GO composites

The α-Fe_2O_3/GO composites were synthesized as follows. 0.05 g GO was dispersed into 50 mL distilled water and the solution was ultrasonicated for 3 h. 4.8654 g $FeCl_3 \cdot 6H_2O$ was dissolved in the solution with vigorous stirring for 0.5 h. Afterward, the aqueous solution of 10 mL HCl (1 M) was added into the above solution, then 12 mmol urea and 2.5 mL ethylene glycol were added into the solution with continuous stirring for 0.5 h. After that, the resultant solution was put into a Teflon-lined stainless steel autoclave of 100 mL capacity, which was sealed and maintained at 180 °C for 12 h. After cooling to room temperature naturally, the resulting product was separated by suction filtration and rinsed with distilled water and ethanol several times to remove the excess $FeCl_3$, and then dried at 60 °C for 5 h under vacuum, resulting in the formation of the final products.

Characterizations

The crystalline phase structures of the prepared α-Fe_2O_3 and α-Fe_2O_3/GO samples were determined by X-ray diffraction (XRD, RIGAKU, Dmax22000) with Cu Kα radiation ($\lambda = 0.15418$ nm) over the 2θ range of 20°–80°. The morphology of the samples was investigated by transmission electron microscopy (TEM, FEI Tecnai $G^2$20). Moreover, high-resolution transmission electron microscopy (HRTEM, JEOL-2010 system at 200 kV), and selected area electron diffraction (SAED, Tecnai G220) were used to characterize the structure of nanocrystals. Surface imaging of the GO sheets was carried out using NT–MDT Solver PRO atomic force microscope (AFM) in tapping mode. In order to take images, samples were initially dispersed in ethanol solution and spray-coated on a freshly cleaved mica surface using a fine atomizer. The amount of GO species was determined by inductive coupling plasma (ICP) IPS-AEC (Optima 2000 DV, Perkin Elmer, USA). Surface area of the samples was determined by Brunauer-Emmet-Teller (BET). N_2 gas adsorption–desorption isotherms were obtained at 77 K on a Micromeritics ASAP-2000 equipment. Samples were precedently degassed at 400 °C. Pore size distributions were calculated by the

BJH model. Light absorption property was examined using a UV–Vis diffuse reflectance spectrophotometer (JASCO, UV-550). Raman spectra of synthesized samples were recorded using Raman spectroscopy (Renishaw, InVia) at 632.8 nm laser radiations. The XPS data were recorded using an ESCALAB250 electron spectrometer using achromatic Al Kα radiation (1,486.6 eV) with Ar^+ sputtering to remove the surface layer of the sample.

Photocatalytic performance study of the α-Fe_2O_3 and α-Fe_2O_3/GO samples

In situ FT-IR spectra were collected with a Fourier Transform Infrared Spectrophotometer (BRUKER VERTEX 70 Optics) and a home-made in situ IR quartz photoreaction cell (Zheng et al. 2009). The photocatalyst was illuminated by an 500 W xenon lamp. The distance between the lamp and sample was about 15 cm. The light intensity at the sample holder was about 40.5 mW cm^{-2}. Two pellets were prepared in parallel.

The reaction cell was purged by dry air for 1 h. After 1 h, the flux of dry air was set at 20 mL/min. Spectra of the clean catalyst surface were collected after this process and utilized as the background. Subsequently, toluene species was fed at the flow rate of 2 μL h^{-1} for ca. 30 min using a syringe pump to a mixing tee where it was vaporized and mixed with the dry air. The reactant mixture then flowed through the reaction cell and allowed to equilibrate at room temperature (293 K). We determined whether the reactant concentration was stabilized by keeping on collecting its infrared spectrum every 5 min until a stable peak line on the infrared spectrum was obtained. Once the reactant concentration was stabilized, the inlet and outlet ports were shut off and the lamps were turned on. The infrared spectra were continuously collected during the reaction. The infrared spectra were collected with a resolution of 1 cm^{-1} and 20 scans in the region of 4,000–1,000 cm^{-1}.

The reactant concentration was measured by gas chromatography (Aligent 7890A, USA). During the reaction process, samples of approximately 1 μL at the outlet every 0.5 h were collected and the change in concentration of toluene was analyzed by a gas chromatography equipped with FID (HP-5 capilary column (30 m × 320 μm × 0.25 m)) and TCD (Porapak Q). When the peak intensity of toluene did not obviously change, the xenon lamp was turned off and the cell was purified with nitrogen.

Results and discussion

XRD analysis

Figure 1 shows the XRD patterns of the natural graphite, GO, α-Fe_2O_3, and α-Fe_2O_3/GO composite. The natural graphite shows a diffraction at $2\theta = 25.6°$, corresponding to the crystal planes of graphene (*d*-spacing of 3.35 Å) (Wang et al. 2011a). The pattern of GO has a peak centered at $2\theta = 10.65°$, corresponding to the (002) inter-planar spacing of 9.235 Å (Xu et al. 2008). The α-Fe_2O_3/GO composite and α-Fe_2O_3 possess sharp diffraction peaks at 2θ of 24.18°, 33.15°, 35.75°, 40.93°, 49.43°, 54.02°, 57.56°, 62.51°, 64.05°, 71.94°, and 75.48° corresponding to (012), (104), (110), (113), (024), (116), (018), (214), (300), (1010), and (220) crystallographic nucleation planes of hematite phase, respectively, which can be indexed to rhombohedral structure α-Fe_2O_3 (JCPDS 84-0311) (Li et al. 2011). These results indicate that α-Fe_2O_3/GO composite with relatively high crystal purity is synthesized. It can be observed that diffraction peaks of bare α-Fe_2O_3 have stronger intensity than those of α-Fe_2O_3/GO composite.

As calculated from the XRD line broadening of the (104) peak using the Scherrer equation $D = 0.89\lambda/\beta\cos\theta$, the average crystallite sizes of the α-Fe_2O_3 and

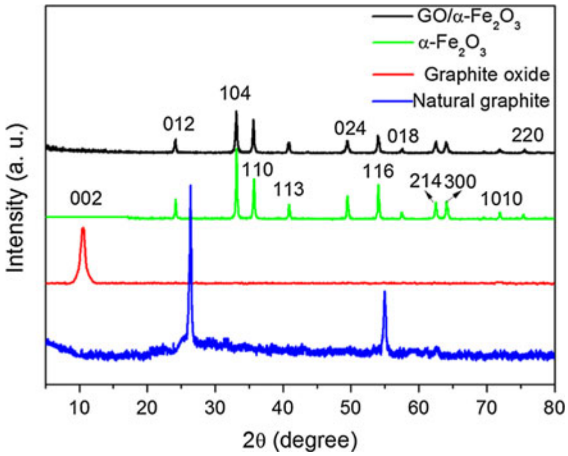

Fig. 1 The X-ray diffraction patterns of the α-Fe_2O_3, graphite, GO, and α-Fe_2O_3/GO samples

α-Fe_2O_3/GO samples are ca. 27 and 24 nm, respectively. The broader peaks of α-Fe_2O_3/GO composite further indicate their smaller average crystallite size, although it is not obvious.

AFM, TEM, and ICP analysis

An AFM image of the GO sample is shown in Fig. 2a. The image of GO shows two pieces of monolayer with thickness of about 2.0 nm. The TEM image in Fig. 2b shows the morphology of the pure α-Fe_2O_3 sample. The α-Fe_2O_3 sample is composed of "spindle-like" microparticles with the dimension sizes around one micrometer. Statistical analysis of dimensional distribution based on low-resolution TEM images indicates that the length and the width are about 1.5 and 0.5 μm on average, respectively.

Figure 2c shows a low-resolution TEM image of α-Fe_2O_3/GO composite. It can be seen that α-Fe_2O_3 particles are closely anchored on the surface of GO nanosheets. The agglomeration of α-Fe_2O_3 particles is not observed, which confirms that GO nanosheets are uniformly coated with α-Fe_2O_3 particles. The α-Fe_2O_3 particles grew onto the GO nanosheets during the synthesis process and appeared as microballs with sizes of 500–1,000 nm in the produced composite. Even after a long duration of sonication during the preparation of the TEM specimen, the GO nanosheets could act as stable supporting materials for anchoring of α-Fe_2O_3 particles.

The TEM image of Fig. 2d with a higher resolution indicates that the α-Fe_2O_3 microparticles grown on GO were formed through the agglomeration of numerous nanoparticles. The apparent sizes of these constituent

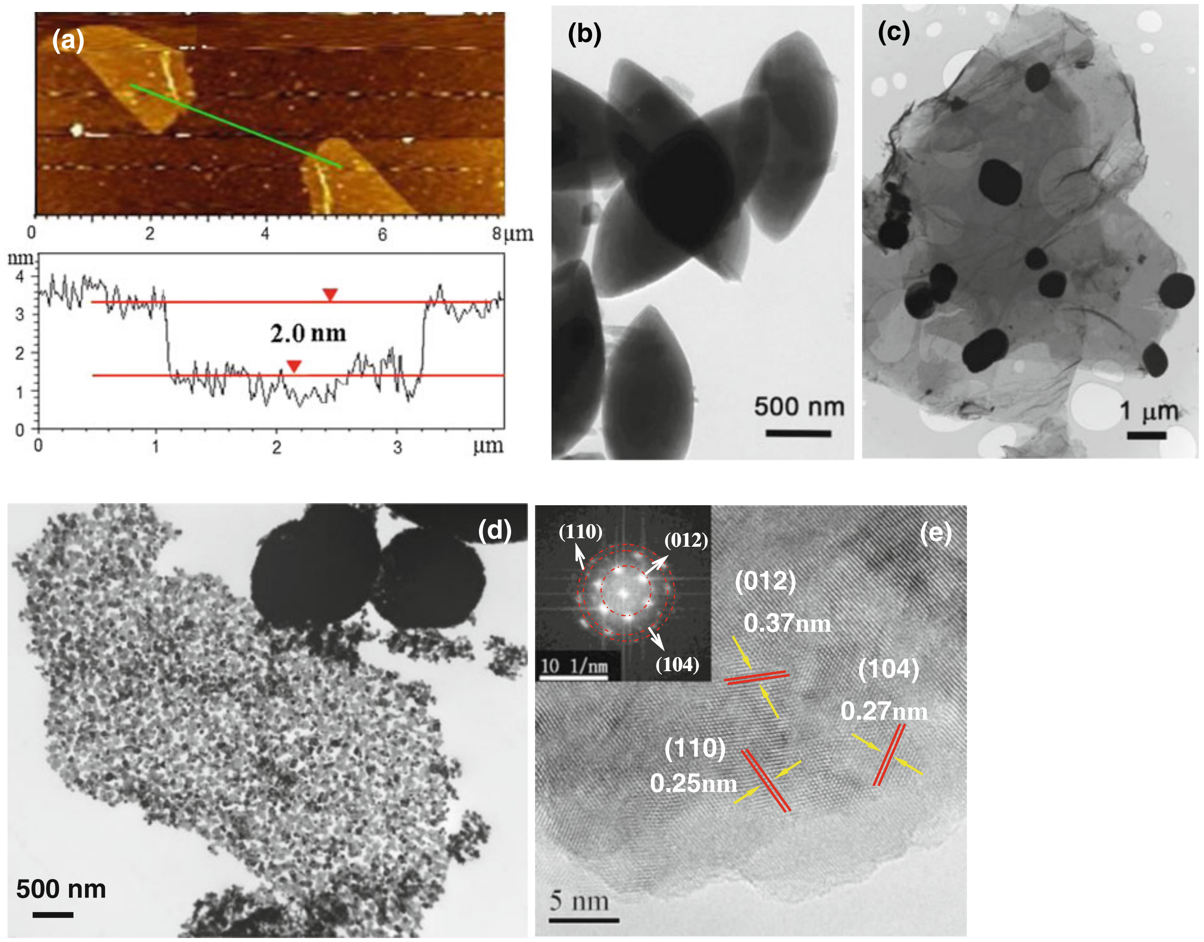

Fig. 2 An AFM image of the GO sample (**a**), the TEM images of the α-Fe_2O_3 sample (**b**) and α-Fe_2O_3/GO sample (**c**) and (**d**), SAED image (*inset*) and HRTEM image of the α-Fe_2O_3/GO sample (**e**)

α-Fe_2O_3 nanoparticles are in the range of about 20–100 nm. This result is consistent with the XRD-determined average crystallite size of ca. 24 nm. The selected area electron diffraction (SAED) pattern (inset of Fig. 2e) of the particles reveals ring patterns corresponding to hematite Fe_2O_3 with rhombohedral crystal structure (JCPDS 89-2810) (Zhu et al. 2011a), while the HRTEM observation (Fig. 2e) of the crystals confirms the same crystal structure. In the HRTEM image (Fig. 2e) of the α-Fe_2O_3/GO sample, the spacings between the lattice fringes are 0.25, 0.27, and 0.37 nm, which is consistent with hematite phase 110, 104, and 012 plane spacing (Reddy et al. 2007), respectively. From the ICP analysis, we know that the composite contains 0.256 wt% GO around the α-Fe_2O_3 particles.

BET analysis

The specific surface area and porosity of the α-Fe_2O_3/GO and Fe_2O_3 samples have been determined and displayed in Table 1. The specific surface areas of the α-Fe_2O_3/GO and α-Fe_2O_3 samples are 70.79 and 12.62 $m^2\ g^{-1}$, respectively. It shows that the GO constituent makes the specific surface area of the sample increase a lot. Analysis of porosity was carried out following the BJH method. The α-Fe_2O_3 and α-Fe_2O_3/GO samples display monomodal pore size distribution with the most frequent pore radii of about 1.67 and 2.18 nm, respectively. The prepared samples are all mesoporous materials according to the distribution of pore sizes. The total pore volumes ($P/P_0 = 0.99$) of the α-Fe_2O_3 and α-Fe_2O_3/GO samples are 0.018 and 0.059 $cm^3\ g^{-1}$, respectively. The sample α-Fe_2O_3/GO has a higher specific surface area and monomodal pore size distribution. These features determining the accessibility of reactant molecules are important for the catalytic performance, which implies that the α-Fe_2O_3/GO composite may have higher catalytic activity than the α-Fe_2O_3 particles.

Table 1 Specific surface area, pore volume data, and pore size distribution of the α-Fe_2O_3/GO and α-Fe_2O_3 samples

Sample	Specific surface area ($m^2\ g^{-1}$)	Pore volume ($cm^3\ g^{-1}$)	Pore size (nm)	Distribution of pore size model
α-Fe_2O_3/GO	70.79	0.059	2.18	Monomodal
α-Fe_2O_3	12.62	0.018	1.67	Monomodal

DRS analysis

The UV–Vis absorption spectra of the α-Fe_2O_3 and α-Fe_2O_3/GO samples are shown in Fig. 3a. A stronger visible light absorption with the same peak at about 574 nm as α-Fe_2O_3 was found for the α-Fe_2O_3/GO composite, which indicates that the carbon sheets could help absorb much more UV–visible light. The introduction of GO into the α-Fe_2O_3 leads to a better utilization of UV–visible light without changing the spectral pattern of α-Fe_2O_3.

Raman spectra analysis

Figure 3b shows the Raman spectra of GO, spindle-like α-Fe_2O_3, and α-Fe_2O_3/GO composite. Two characteristic peaks of the D and G bands from GO could be observed at around 1,330 and 1,580 cm^{-1}. The intensity ratios of D and G band (ID: IG) are 1.21, 1.47, and 1.32, respectively. The more disordered carbon structure in the α-Fe_2O_3/GO composites compared with bare GO may be due to the possible insertion of α-Fe_2O_3 into GO layers (Pumera 2011).

XPS analysis

The electronic structure of spindle-like α-Fe_2O_3 and α-Fe_2O_3/GO composite was investigated by XPS. Figure 4 shows the representative XPS spectra of α-Fe_2O_3 and α-Fe_2O_3/GO composite. The survey spectrum of α-Fe_2O_3/GO reveals the spectroscopic signature of carbon, oxygen, and iron. The Fe $2p_{3/2}$ peak is centered at 721 eV and the Fe $2p_{1/2}$ peak at 707.4 eV. This indicates the oxidation state of Fe^{3+} in the sample (Grosvenor et al. 2004). The oxygen peak with O1s at 526.7 eV and the carbon peak with C 1s at 281.22 eV on the surface are present in the α-Fe_2O_3/GO composite sample. A quantitative analysis of the data in the $Fe2p_{3/2}$, $Fe2p_{1/2}$, and C1s regions allows to estimate the atom ratio of Fe:O:C = 1:2.8:0.22 (Table 2). The above results further indicate the successful preparation of α-Fe_2O_3/GO composite.

Photocatalytic capacity study on α-Fe_2O_3 and α-Fe_2O_3/GO samples

In situ FTIR study provides real-time monitoring of the transient events occurring on the catalyst during the reaction. The spectral information on the adsorption

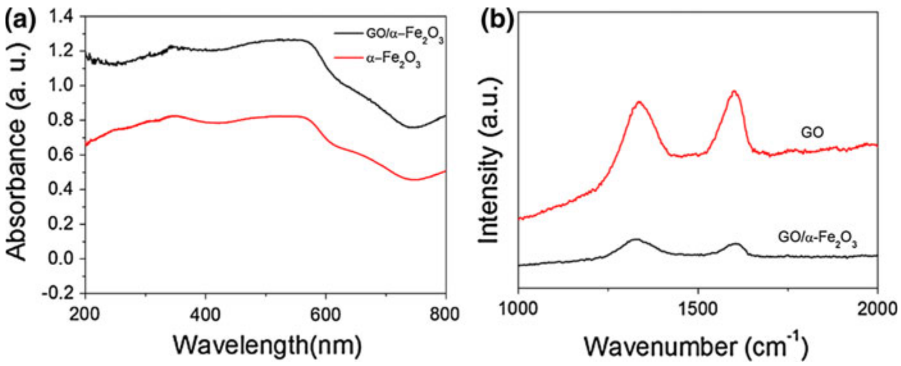

Fig. 3 **a** The UV–Vis absorption spectra of the α-Fe_2O_3 and α-Fe_2O_3/GO samples, and **b** the Raman spectra of the prepared α-Fe_2O_3, GO, and α-Fe_2O_3/GO samples

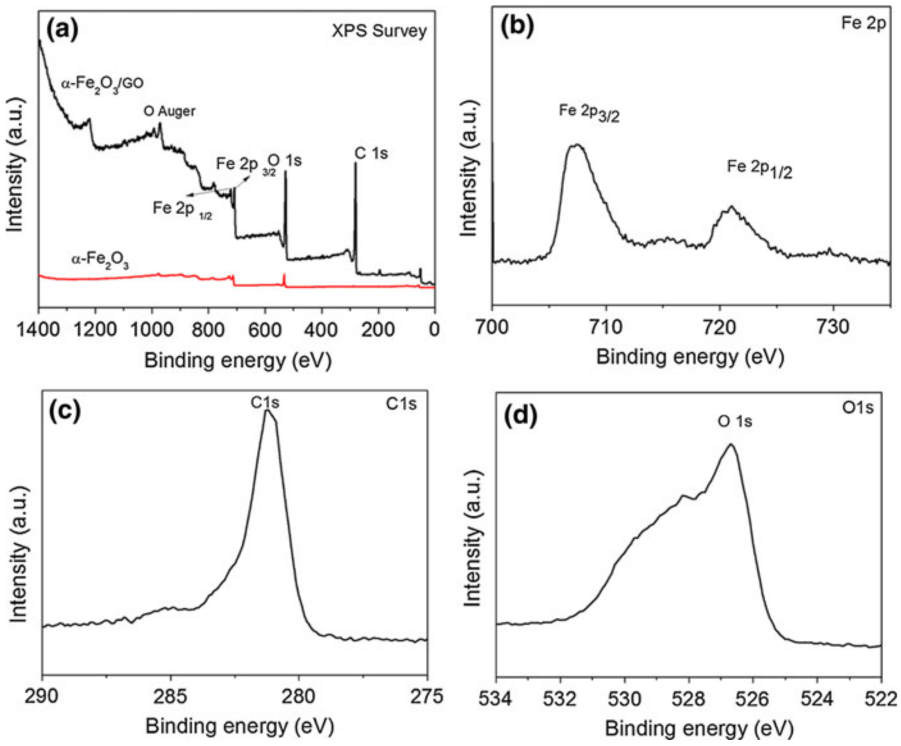

Fig. 4 The whole XPS spectra of the α-Fe_2O_3 and the α-Fe_2O_3/GO samples (**a**), Fe 2p XPS spectrum (**b**), C 1s XPS spectrum (**c**), and O 1s XPS spectrum of the α-Fe_2O_3/GO sample (**d**)

and the photodegradation of toluene over the synthesized α-Fe_2O_3/GO sample and α-Fe_2O_3 sample are shown in Fig. 5. Upon toluene entering the reaction cell, the intensities of the characteristic peaks for toluene increased quickly. After 25 min, the intensities of peaks for toluene over α-Fe_2O_3/GO sample decreased slowly and had a steady trend (Fig. 5a). For the α-Fe_2O_3 sample, the adsorption/desorption processes equilibrated in 60 min (Fig. 5b). Then the inlet and outlet ports were shut off. The initial concentration of the toluene was determined as about 750 mg m^{-3} by gas chromatography.

Table 2 The results of XPS analysis for the α-Fe_2O_3/GO sample

Element	Electronic energy (eV)	Atom ratio (%)
Fe $2p_{3/2}$	726	
Fe $2p_{1/2}$	712.7	24.81
O 1s	531.6	69.78
C 1s	288.76	5.41

During xenon-lamp illumination, a set of infrared transmission spectra were collected during the photocatalytic degradation of toluene over the α-Fe_2O_3/GO

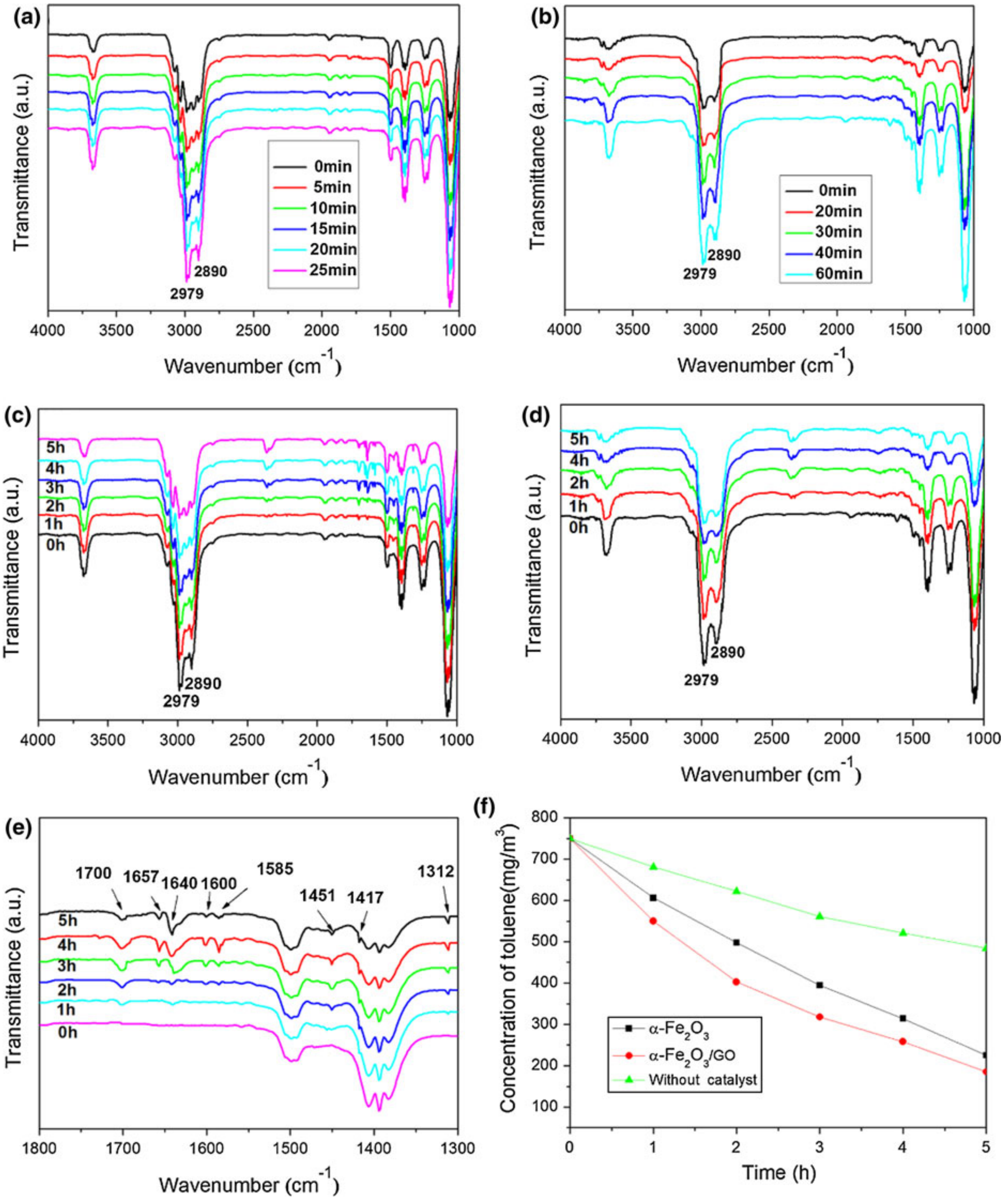

Fig. 5 The infrared transmittance spectra of toluene adsorbed onto the α-Fe_2O_3/GO (**a**) and α-Fe_2O_3 samples (**b**) under dark condition, the infrared transmittance spectra for toluene degradation over the α-Fe_2O_3 (**c**) and the α-Fe_2O_3/GO samples (**d**, **e**) under 5 h irradiation by xenon lamp, and the comparison on the toluene degradation results using the catalysts and without any catalyst (**f**)

sample and α-Fe_2O_3 sample. Figure 5c–e displays the spectra for toluene photodegradation over α-Fe_2O_3/GO sample and α-Fe_2O_3 sample for 5-h illumination. Prior to xenon-lamp illumination ($t = 0$), the spectrum displays the characteristic toluene bands at 2,979 and 2,890 cm^{-1} (Fig. 5c, d). Upon irradiation, the intensity of these bands began to decrease slowly. The bands at 2,360 cm^{-1} and 2,340 cm^{-1} corresponding to CO_2 (Fig. 5c, d) and H_2O (1,640 cm^{-1}) (Fig. 5c, d) increased as the reaction proceeded.

The color of catalysts was observed to change from brown to black. This degeneration of catalysts may be related to some new surface species, which could be explained by the FTIR spectra in Fig. 5e. Some bands are related to the adsorbed water and hydroxyl groups in the range of 1,300–1,700 cm^{-1} (bands around 1,657, 1,495, 1,451, 1,417, and 1,312 cm^{-1}) (Fig. 5e). Similar bands have been reported for benzaldehyde adsorption on nanostructured TiO_2 and Degussa P25 (Mendez-Roman and Cardona-Martinez 1998; Martra 2000). These results indicate that weakly adsorbed benzoic acid was formed as the reaction proceeded (Morterra 1988). Benzoic acid molecules resulting from the photo-oxidation of toluene interact with the catalyst surface weakly, so that they can be released to the gas phase. By contrast, hydroxyl groups on the surface of α-Fe_2O_3 microparticles are able to react with benzoic acid (Marcì et al. 2003), which is adsorbed on the surface of α-Fe_2O_3 microparticles, leading to the progressive deactivation of the catalyst in the gas–solid system.

Meanwhile, we detected the concentration change of toluene by gas chromatography during xenon-lamp illumination. Toluene was sampled each 0.5 h. The initial concentration of toluene measured by gas chromatography was 750 mg m^{-3}. Figure 5f shows the comparison between the concentration changes of toluene by 5-h illumination over α-Fe_2O_3, α-Fe_2O_3/GO sample, and without any catalyst. After 5-h prolonged irradiation, degradation percentages of toluene over the α-Fe_2O_3, α-Fe_2O_3/GO sample, and without any catalyst reached to 70, 75, and 36 %, respectively. The α-Fe_2O_3/GO composite with sparser distribution of α-Fe_2O_3 particles could exhibit a little higher photocatalytic activity than the α-Fe_2O_3 sample, even though the α-Fe_2O_3 content in α-Fe_2O_3/GO composite is diluted by the two nanometer-thick carbon sheets.

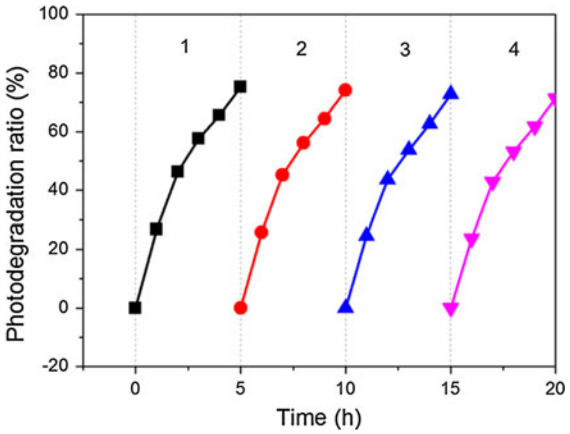

Fig. 6 Cyclic photodegradation of toluene by the α-Fe_2O_3/GO sample

The stability of the catalyst α-Fe_2O_3/GO

The stability test about the catalyst α-Fe_2O_3/GO has been done under the same in situ FT-IR test condition for four reaction cycles. The photodegradation ratio of the substrate was measured as a function of time. The results are shown in Fig. 6. It was found that the photodegradation ratio of toluene reached to 71 % after the fourth repetition over the catalyst α-Fe_2O_3/GO, which was slightly lower than that (75 %) with the fresh catalyst. This result shows that the α-Fe_2O_3/GO catalyst has good stability and reusability.

Conclusions

In summary, α-Fe_2O_3/GO composite was prepared via a simple hydrothermal and Hummers' method. The possible growth of α-Fe_2O_3 onto GO layers led to a higher absorbance capacity for visible light by α-Fe_2O_3/GO composite than α-Fe_2O_3 microparticles. Comparing the photocatalytic oxidation of gaseous toluene over the samples, the prepared α-Fe_2O_3/GO composite was more active than α-Fe_2O_3. Weakly adsorbed benzaldehyde and benzoic acid could be formed on the catalyst surface. The hydroxyl groups played a key role during the photocatalytic process, and the dehydroxylation should be responsible for the deactivation of the composite in a long-term reaction. The composite of α-Fe_2O_3/GO could be promisingly utilized in photo-aided air purification as a green catalyst.

Acknowledgments This work was supported financially by the National Nature Science Foundation of China (NSFC-RGC 21061160495 and No. 21207015), the National High Technology Research and Development Program of China (863 Program) (No. 2010AA064902), the Major State Basic Research Development Program of China (973 Program) (No. 2011CB936002), the Excellent Talents Program of Liaoning Provincial University (LR2010090), and the Key Laboratory of Industrial Ecology and Environmental Engineering, China Ministry of Education.

References

Akhavan O, Ghaderi E, Esfandiar A (2011) Wrapping bacteria by graphene nanosheets for isolation from environment, reactivation by sonication, and inactivation by near-infrared irradiation. J Phys Chem B 115:6279–6288

Beermann N, Vayssieres L, Lindquist SE, Hagfeldt A (2000) Photoelectrochemical studies of oriented nanorod thin films of hematite. J Electrochem Soc 147:2456–2461

Cesar I, Kay A, Gonzalez Martinez JA, Grätzel M (2006) Translucent thin film Fe_2O_3 photoanodes for efficient water splitting by sunlight: nanostructure-directing effect of Si-doping. J Am Chem Soc 128:4582–4583

Chauhan P, Annapoorni S, Trikha SK (1999) Humidity-sensing properties of nanocrystalline hematite thin films prepared by sol-gel processing. Thin Solid Films 346:266–268

Chen J, Xu LN, Li WY, Gou XL (2005) α-Fe_2O_3 nanotubes in gas sensor and lithium-ion battery applications. Adv Mater 17:582–586

Chen D, Tang LH, Li JH (2010a) Graphene-based materials in electrochemistry. Chem Soc Rev 39:157–3180

Chen JS, Zhu TX, Yang H, Yang HG, Lou XW (2010b) Top-down fabrication of α-Fe_2O_3 single-crystal microstructures with controlled porosity for enhanced lithium storage capabilities. J Am Chem Soc 132:13162–13164

Chou SL, Wang JZ, Choucair M, Liu HK, Stride JA, Dou SX (2010) Enhanced reversible lithium storage in a nanosize silicon/graphene composite. Electrochem Commun 12: 303–306

Dong XC, Shi YM, Huang W, Chen P, Li LJ (2010) Electrical detection of DNA hybridization with single-base specificity using transistors based on CVD-grown graphene sheets. Adv Mater 22:1649–1653

Fan ZY, Wen XG, Yang SH, Lu JG (2005) Controlled p- and n-type doping of Fe_2O_3 nanobelt field effect transistors. Appl Phys Lett 87:013113

Geim AK, Novoselov KS (2007) The rise of graphene. Nat Mater 6:183–191

Gou XL, Wang GX, Kong XY, Wexler D, Horvat J, Yang J, Park J (2008) Flutelike porous hematite nanorods and branched nanostructures: synthesis, characterisation and application for gas-sensing. Chem Eur J 14:5996–6002

Grosvenor AP, Kobe BA, Biesinger MC, Mclntyre NS (2004) Investigation of multiplet splitting of Fe 2p XPS spectra and bonding in iron compounds. Surf Interface Anal 36: 1564–1574

Guo CX, Zheng XT, Lu ZS, Lou XW, Li CM (2010) Biointerface by cell growth on layered graphene-artificial peroxidase-protein nanostructure for in situ quantitative molecular detection. Adv Mater 22:5164–5167

Hsu LC, Li YY, Hsiao CY (2008) Synthesis, electrical measurement, and field emission properties of α-Fe_2O_3 nanowires. Nanoscale Res Lett 3:330–337

Hsu LC, Kuo YP, Li YY (2009) On-chip fabrication of an individual α-Fe_2O_3 nanobridge and application of ultra-wide wavelength visible-infrared photodetector/optical switching. Appl Phys Lett 94:133108

Hu XL, Yu JC, Gong JM, Li Q, Li GS (2007) α-Fe_2O_3 nanorings prepared by a microwave-assisted hydrothermal process and their sensing properties. Adv Mater 19:2324–2329

Hummers WS, Offeman RE (1958) Preparation of graphitic oxide. J Am Chem Soc 80:1339

Ji LW, Tan ZK, Kuykendall TR, Aloni S, Xun SD, Lin E, Battagli V, Zhang YG (2011) Fe_3O_4 nanoparticle-integrated graphene sheets for high-performance half and full lithium ion cells. Phys Chem Chem Phys 13:7170–7177

Kim JY, Jang JW, Youn DH, Kim JY, Kim ES, Lee JS (2012) Graphene–carbon nanotube composite as an effective conducting scaffold to enhance the photoelectrochemical water oxidation activity of a hematite film. RSC Adv 2:9415–9422

Lee JK, Smith KB, Hayner CM, Kung HH (2010) Silicon nanoparticles–graphene paper composites for Li ion battery anodes. Chem Commun 46:2025–2027

Li XL, Wei WJ, Wang SZ, Kuai L, Geng BY (2011) Single-crystalline α-Fe_2O_3 oblique nanoparallelepipeds: high-yield synthesis, growth mechanism and structure enhanced gas-sensing properties. Nanoscale 3:718–724

Li H, Zhao QD, Li XY, Shi Y, Chen GH (2012) Fabrication and surface photovoltage study of hematite microparticles with hollow spindle-shaped structure. Appl Surf Sci 258: 7099–7104

Lian PC, Zhu XF, Xiang HF, Li Z, Yang WS, Wang HH (2010) Enhanced cycling performance of Fe_3O_4–graphene nanocomposite as an anode material for lithium-ion batteries. Electrochim Acta 56:834–840

Liang YY, Wang HL, Casalongue HS, Chen Z, Dai HJ (2010) TiO_2 nanocrystals grown on graphene as advanced photocatalytic hybrid materials. Nano Res 3:701–705

Liu Z, Robinson JT, Sun X, Dai H (2008) Pegylated nano graphene oxide for delivery of water-insoluble cancer drugs. J Am Chem Soc 130:10876–10877

Liu H, Wang GX, Park J, Wang JZ, Liu HK (2009) Electrochemical performance of alpha-Fe_2O_3 nanorods as anode material for lithium-ion cells. Electrochim Acta 54: 1733–1736

Liu J, Bai H, Wang Y, Liu Z, Zhang X, Sun DD (2010) Self assembling TiO_2 nanorods on large graphene oxide sheets at a two-phase interface and their anti-recombination in photocatalytic applications. Adv Funct Mater 20: 4175–4181

Marcì G, Addamo M, Augugliaro V, Coluccia S, García-López E, Loddo V, Martra G, Palmisano L, Schiavello M (2003) Photocatalytic oxidation of toluene on irradiated TiO_2: comparison of degradation performance in humidified air, in water and in water containing a zwitterionic surfactant. J Photochem Photobio A 160:105–114

Martra G (2000) Lewis Acid and base sites at the surface of microcrystalline TiO_2 anatase: relationships between surface morphology and chemical behaviour. Appl Catal A General 200:275–282

Mendez-Roman R, Cardona-Martinez N (1998) Relationship between the formation of surface species and catalyst deactivation during the gas-phase photocatalytic oxidation of toluene. Catal Today 40:353–365

Meng F, Li J, Cushing SK, Bright J, Zhi M, Rowley JD, Hong Z, Manivannan A, Bristow AD, Wu N (2013) Photocatalytic water oxidation by hematite/reduced graphene oxide composites. ACS Catal 3:746–751

Miao X, Tongay S, Petterson MK, Berke K, Rinzler AG, Appleton BR, Hebard AF (2012) High efficiency graphene solar cells by chemical doping. Nano Lett 12:2745–2750

Morterra C (1988) An infrared spectroscopic study of anatase properties. Part 6. Surface hydration and strong Lewis acidity of pure and sulphate-doped preparations. J Chem Soc, Faraday Trans 84:1617–1637

Mukherjee S, Kaloni TP (2012) Electronic properties of boron- and nitrogen-doped graphene: a first principles study. J Nanopart Res 14:1059

Novoselov KS, Jiang D, Schedin F (2005) Two-dimensional atomic crystals. J Proc National Acad Sci 102:10451–10453

Nuli Y, Zeng R, Zhang P (2008) Controlled synthesis of alpha-Fe_2O_3 nanostructures and their size-dependent electrochemical properties for lithium-ion batteries. J Power Sources 184:456–461

Park S, Ruoff RS (2009) Chemical methods for the production of graphenes. Nat Nanotechnol 4:217–224

Pumera M (2011) Graphene-based nanomaterials for energy storage. Energy Environ Sci 4:668–674

Reddy MV, Yu T, Sow CH (2007) α-Fe_2O_3 nanoflakes as an anode material for li-ion batteries. Adv Funct Mater 17:2792–2799

Shen L, Yuan C, Luo H, Zhang X, Yang S, Lu X (2011) In situ synthesis of high-loading $Li_4Ti_5O_{12}$–graphene hybrid nanostructures for high rate lithium ion batteries. Nanoscale 3:572–574

Song HJ, Qian J, Jia XH, Yang XF, Tang H, Min CY (2012) A new one-step synthesis method for coating multi-walled carbon nanotubes with iron oxide nanorods. J Nanopart Res 14:698

Sun YQ, Wu QO, Shi GQ (2011) Graphene based new energy materials. Energy Environ Sci 4:1113–1132

Wang DH, Choi DW, Li J, Yang ZG, Nie ZM, Kou R, Hu DH, Wang CM, Saraf LV, Zhang JG, Aksay IA, Liu J (2009) Self-Assembled TiO_2-graphene hybrid nanostructures for enhanced Li-ion insertion. ACS Nano 3:907–914

Wang DH, Kou R, Choi DW, Yang ZG, Nie ZM, Li J, Saraf LV, Hu DH, Zhang JG, Graff GL, Liu J, Pope MA, Aksay IA (2010a) Ternary self-assembly of ordered metal oxide–graphene nanocomposites for electrochemical energy storage. ACS Nano 4:1587–1595

Wang HL, Casalongue HS, Liang YY, Dai HJ (2010b) $Ni(OH)_2$ Nanoplates grown on graphene as advanced electrochemical pseudocapacitor materials. J Am Chem Soc 132:7472–7477

Wang Y, Shi R, Lin J, Zhu Y (2010c) Significant photocatalytic enhancement in methylene blue degradation of TiO_2 photocatalysts via graphene-like carbon in situ hybridization. Appl Catal B 100:179–183

Wang G, Liu T, Luo YJ, Zhao Y, Zhao YR, Bai JB, Wang H (2011a) Preparation of Fe_2O_3/graphene composite and its electrochemical performance as an anode material for lithium ion batteries. J Alloys Comp 509:216–220

Wang JZ, Zhong C, Wexler D, Idris NH, Wang ZX, Chen LQ, Liu HK (2011b) Graphene-encapsulated Fe_3O_4 nanoparticles with 3D laminated structure as superior anode in lithium ion batteries. Chem Eur J 17:661–667

Wu XL, Guo YG, Wan LJ (2008) α-Fe_2O_3 nanostructures: inorganic salt-controlled synthesis and their electrochemical performance toward lithium storage. J Phys Chem C 112:16824–16829

Wu ZS, Ren WC, Wen L, Gao LB, Zhao JP, Chen ZP, Zhou GM, Li F, Cheng HM (2010) Graphene anchored with Co_3O_4 nanoparticles as anode of lithium ion batteries with enhanced reversible capacity and cyclic performance. ACS Nano 4:3187–3194

Xu YX, Bai H, Lu GW, Li C, Shi GQ (2008) Flexible graphene films via the filtration of water-soluble noncovalent functionalized graphene sheets. J Am Chem Soc 130: 5856–5857

Yang XY, Zhang XY, Ma YF, Huang Y, Wang YS, Chen YS (2009) Superparamagnetic graphene oxide-Fe_3O_4 nanoparticles hybrid for controlled targeted drug carriers. J Mater Chem 19:2710–2714

Yoo D, Cuong TV, Pham VH, Chung JS, Khoa NT, Kim EJ (2011) Enhanced photocatalytic activity of GO decorated on TiO_2 films under UV and visible irradiation. Curr Appl Phys 1:805–808

Yu T, Zhu Y, Xu X, Yeong KS, Shen Z, Chen P, Lim CT, Thong JT, Sow CH (2006) Substrate-friendly synthesis of metal oxide nanostructures using a hotplate. Small 2:80–84

Zhang H, Lv X, Li Y, Wang Y, Li J (2010a) P25–graphene composite as a high performance photocatalyst. ACS Nano 4:380–386

Zhang J, Liu XH, Guo XZ, Wu SH, Wang SR (2010b) A general approach to fabricate diverse noble-metal (Au, Pt, Ag, Pt/Au)/Fe_2O_3 hybrid nanomaterials. Chem Eur J 16: 8108–8116

Zhang M, Lei D, Yin X, Chen L, Li Q, Wang Y, Wang T (2010c) Magnetite/graphene composites: microwave irradiation synthesis and enhanced cycling and rate performances for lithium ion batteries. J Mater Chem 20:5538–5543

Zhang JT, Jiang JW, Zhao XS (2011) Synthesis and capacitive properties of manganese oxide nanosheets dispersed on functionalized graphene sheets. J Phys Chem C 115: 6448–6454

Zheng CL, Li XY, Zhao QD, Qu ZP, Quan X (2009) Photo-oxidation of gas-phase cyclohexane species over nanostructured TiO_2 fabricated by different strategies. Sep Purif Technol 67:326–330

Zhou GM, Wang DW, Li F (2010) Graphene-wrapped Fe_3O_4 anode material with improved reversible capacity and cyclic stability for lithium ion batteries. Chem Mater 22: 5306–5313

Zhu JX, Zhu T, Zhou XZ, Zhang YY, Lou XW, Chen XD, Zhang H, Hng HH, Yan QY (2011a) Facile synthesis of metal oxide/reduced graphene oxide hybrids with high lithium storage capacity and stable cyclability. Nanoscale 3:1084–1089

Zhu X, Zhu Y, Murali S, Stoller MD, Ruoff RS (2011b) Nanostructured reduced graphene oxide/Fe_2O_3 composite as a high-performance anode material for lithium ion batteries. ACS Nano 5:3333–3338